

A Sensorimotor Circuit in Mouse Cortex for Visual Flow Predictions

Highlights

- Mouse A24b/M2 sends a dense topographically organized input to V1
- Motor-related signals from A24b/M2 drive motor and mismatch signals in V1
- Training to navigate a left-right inverted world reverses A24b/M2 visuomotor coding
- Stimulation of A24b/M2 axons in V1 in navigating mice elicits turning behavior

Authors

Marcus Leinweber, Daniel R. Ward,
Jan M. Sobczak, Alexander Attinger,
Georg B. Keller

Correspondence

georg.keller@fmi.ch

In Brief

Top-down input to visual cortex from prefrontal areas is involved in attentional and contextual modulation of sensory responses. Leinweber et al. argue that, in the mouse, top-down input to V1 from A24b/M2 carries a prediction of visual flow given movement.

A Sensorimotor Circuit in Mouse Cortex for Visual Flow Predictions

Marcus Leinweber,¹ Daniel R. Ward,¹ Jan M. Sobczak,^{1,3} Alexander Attinger,^{1,2} and Georg B. Keller^{1,2,4,*}

¹Friedrich Miescher Institute for Biomedical Research, Basel, Switzerland

²Faculty of Natural Sciences, University of Basel, Basel, Switzerland

³Present address: Brain Research Institute, University of Zurich, Zurich, Switzerland

⁴Lead Contact

*Correspondence: georg.keller@fmi.ch

<http://dx.doi.org/10.1016/j.neuron.2017.08.036>

SUMMARY

The cortex is organized as a hierarchical processing structure. Feedback from higher levels of the hierarchy, known as top-down signals, have been shown to be involved in attentional and contextual modulation of sensory responses. Here we argue that top-down input to the primary visual cortex (V1) from A24b and the adjacent secondary motor cortex (M2) signals a prediction of visual flow based on motor output. A24b/M2 sends a dense and topographically organized projection to V1 that targets most neurons in layer 2/3. By imaging the activity of A24b/M2 axons in V1 of mice learning to navigate a 2D virtual environment, we found that their activity was strongly correlated with locomotion and resulting visual flow feedback in an experience-dependent manner. When mice were trained to navigate a left-right inverted virtual environment, correlations of neural activity with behavior reversed to match visual flow. These findings are consistent with a predictive coding interpretation of visual processing.

INTRODUCTION

Visual processing in cortex is often described as a feedforward hierarchy of increasingly complex representations that functions to extract objects from visual input (Felleman and Van Essen, 1991; Marr, 1982; Riesenhuber and Poggio, 1999). In this framework, top-down or “feedback” signals are thought to modulate visual responses based on visual representations in higher levels of the hierarchy. This modulation can be driven by attention (Roelfsema et al., 1998; Zhang et al., 2014), context (Fiser et al., 2016; Zipser et al., 1996), or expectations (Gilbert and Li, 2013; Gilbert and Sigman, 2007). A mechanistic interpretation of these top-down signals is predictive coding (Rao and Ballard, 1999; Spratling, 2010). This theory postulates that a prediction of the component features based on visual representations in higher levels of the hierarchy is sent to lower levels, where it is compared to feedforward signals to compute mismatch between the two. Predictions are computed based on an internal

model of the environment that is updated by mismatches fed forward from lower levels of the hierarchy. Predictive coding is a central idea in a whole family of theories of brain function (Barlow, 1994; Clark, 2013; Friston, 2010; Hawkins and Blakeslee, 2004; Wolpert et al., 1995).

Evidence for predictive coding in primary visual cortex (V1) has come mainly from its ability to explain non-classical visual response properties of V1 neurons (Grosof et al., 1993; Rao and Ballard, 1999; Spratling, 2010). One of the central problems with testing the hypothesis of predictive coding is that predictions are difficult to constrain experimentally. Typically, this is attempted using learned associations between behavior and sensory feedback. For example, sensory feedback couples in a predictable way to motor output. Hence, the experimental assumption is that signals generated during movement that are fed back to sensory areas should constitute an experience-dependent prediction of sensory feedback. This is referred to as an efference copy in the theory of internal models (Blakemore et al., 2000; von Holst and Mittelstaedt, 1950; Jordan and Rumelhart, 1992). Using paradigms of sensorimotor coupling, it has been demonstrated that layer 2/3 of sensory cortices signals a mismatch between predicted and actual sensory feedback (Eliades and Wang, 2008; Keller et al., 2012). The source of the motor-related prediction necessary to generate these mismatch signals is, however, still unknown.

Locomotion is sufficient to drive activity in mouse V1 (Keller et al., 2012; Saleem et al., 2013) and has been shown to modulate visually evoked activity (Niell and Stryker, 2010). Two hypotheses for the function of these motor-related signals are a gain modulation of visual responses (Ayaz et al., 2013; Fu et al., 2014; Niell and Stryker, 2010) and a prediction of visual flow based on motor output (Keller et al., 2012). Gain modulation of visual responses could be mediated by a low-dimensional signal such as a neuromodulatory input. A prediction of visual flow, on the other hand, would require a dense long-range excitatory input capable of conveying a high-resolution signal. Compatible with the idea of gain modulation, both cholinergic (Fu et al., 2014) and noradrenergic (Polack et al., 2013) inputs to V1 have been described. These neuromodulatory inputs drive locomotion-related gain changes in V1. However, the idea of neuromodulatory gain modulation during movement, acting through a disinhibitory circuit (Fu et al., 2014), cannot account for locomotion-driven activity in the complete absence of visual input (Keller et al., 2012; Pakan et al., 2016; Saleem

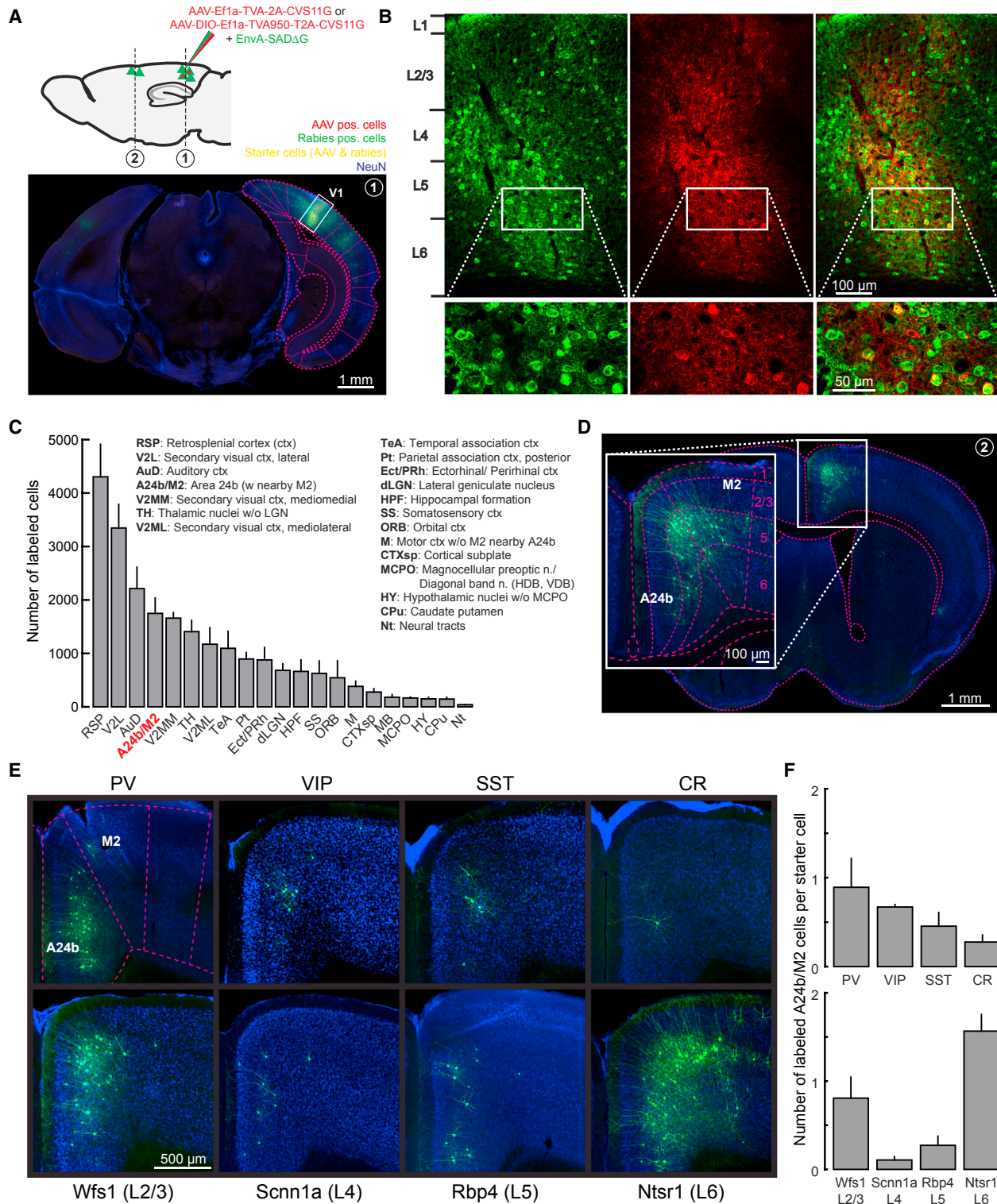


Figure 1. A24b/M2 Is One of the Main Inputs to V1 and Primarily Targets Layer 2/3 and 6 Excitatory Neurons as well as PV Interneurons

(A) Top: Injection scheme for monosynaptic input mapping experiments using rabies virus. Vertical dashed lines indicate position of coronal sections in (A) and (D). Bottom: Coronal section ($\lambda = 0.25$ mm) through an injection site in V1. AAV-positive cells are labeled in red, and rabies-positive cells are labeled in green. NeuN staining is in blue.

(legend continued on next page)

et al., 2013) or the context dependence of gain modulation (Pakan et al., 2016).

Here, we hypothesize that top-down projections to V1 carry a prediction of visual input based on motor output. The motor command for a left turn, for example, would lead to a prediction of full-field visual flow to the right. Generating a prediction of visual flow would thus require a transformation of the motor command to a signal in visual coordinates. In the framework of internal models, this transformation from motor coordinates (which muscles are activated) to sensory coordinates (how does the visual stimulus change) is referred to as a forward model (Wolpert et al., 1995). Anatomically, this could be implemented in different ways. A motor-related brain area could send an efference copy of the motor command to visual cortex in motor coordinates, and the connectivity between axons from the motor-related area and visual neurons could act as the forward model, transforming the signal to visual coordinates. Alternatively, the motor command could be transformed to visual coordinates in upstream areas and sent to visual cortex in visual coordinates. These two possibilities can be disambiguated by recording from axons of motor-related areas in visual cortex.

We sought to identify top-down inputs to V1 that could convey a prediction of visual flow based on motor output. One candidate area is the anterior cingulate cortex (ACC) (Miller and Vogt, 1984; Vogt and Miller, 1983; Zhang et al., 2014, 2016), which is bidirectionally connected with the adjacent secondary motor cortex (Vogt and Miller, 1983). Stimulation of ACC in rats causes head and eye movements (Sinnamon and Galer, 1984), and recent work demonstrates that the input from ACC to V1 has a role in attentional modulation of visual responses (Zhang et al., 2014) and experience-dependent spatial predictions (Fiser et al., 2016).

If the ACC input to V1 conveys a prediction of visual flow based on the mouse's movements, it should be characterized by a few defining features. First, the projection should have a bandwidth comparable to that of the feedforward visual input, measured either as the number of afferent neurons or as the fraction of V1 neurons targeted. Second, it should convey motor-related activity to V1, such that an inactivation of the input results in a decrease in motor-related activity in V1 neurons. Consequently, visuomotor mismatch signals in V1, which result from a comparison of an excitatory motor-related input and an inhibitory visual input (Attinger et al., 2017; Zmarz and Keller, 2016), should also decrease upon inactivation. Third, activity of this projection should depend on visuomotor experience and adapt to changes in visuomotor coupling as the mouse learns to control

visual feedback in a novel environment. Lastly, artificial stimulation of the projection should result in illusory visual flow.

In the work we present here, we identify A24b, a subdivision of ACC, and an adjacent part of secondary motor cortex (M2), as one origin of a motor-related input to V1 and revisit the question of the function of this top-down projection. We suggest that one component of this top-down input is a prediction of visual flow based on the motor output of the mouse, consistent with the idea that internal models govern the processing of sensory input.

RESULTS

A24b/M2 Is One of the Main Inputs to V1 and Mainly Targets Layer 2/3 and Layer 6 Excitatory Neurons and PV Interneurons

To survey all afferents to V1 and identify potential motor-related input, we used transsynaptic rabies tracing (Wickersham et al., 2007). We injected an adeno-associated virus (AAV; AAV2/1-Ef1a-TVA950-T2A-CVS11G) into V1 to express the rabies virus G protein and the TVA receptor in V1 neurons. Monosynaptic rabies tracing was initiated using an EnvA-coated SAD Δ G rabies virus (Figure 1A). The AAV vector was injected into V1 2 days prior to the injection of the rabies virus at the same location. As the Ef1a promoter used in the AAV virus tends to bias expression to layer 2/3 and layer 5 excitatory neurons (Attinger et al., 2017), tracing was likely also biased to presynaptic input to those neurons. Five days after the rabies virus injection, mice were sacrificed and their brains were sectioned and immunohistologically processed (see STAR Methods). We found an average of $2,179 \pm 877$ (mean \pm SD) labeled starter cells per mouse throughout all layers of V1 (Figure 1B and Movie S1), and $30,437 \pm 6,112$ presynaptic cells throughout the entire brain (three mice). Presynaptic cells were mapped onto brain regions as defined by a mouse brain atlas (Franklin and Paxinos, 2012) (Figure 1C). We found the largest fraction of presynaptic cells in primary ($7,723 \pm 2,124$ cells, or 25%) and secondary visual areas (V2L, V2ML, and V2MM, $6,177 \pm 1,444$ cells, or 20%), followed by retrosplenial ($4,304 \pm 1,055$ cells, or 14%) and auditory cortex ($2,212 \pm 694$ cells, or 7%). The largest input from a motor-related area came from a region of cortex that was composed of A24b ($1,748 \pm 501$ cells, or 6%), a sub-region of the ACC approximately corresponding to the dorsal part of ACC in a region just anterior of bregma (0 mm to +1 mm) (Vogt and Paxinos, 2014), and the medial part of M2 directly adjacent to A24b (Figure 1D). Using a boundary between A24b and M2 as defined in the Franklin and Paxinos mouse brain atlas (Franklin

(B) Top: Magnification of the injection site shown in (A). Left: Cells infected by the rabies virus express GFP and appear green. Middle: Cells infected by the AAV virus were identified by staining against the 2A linker peptide and appear red. Right: Overlay of the green and the red channels. Cells that appear yellow have been infected by both the AAV and the rabies virus and are putative starter cells. Bottom: Magnification of the area indicated by the white rectangle.

(C) Number of cells labeled in different brain regions by rabies tracing from V1 (three mice). Brain regions were identified using a mouse brain atlas (Franklin and Paxinos, 2012). Note: A24b/M2 is one of the largest inputs to V1, with twice as many cells labeled as in the dorsolateral geniculate nucleus (dLGN), the main source of thalamic input to V1. Here and in the following panels, error bars indicate SEM.

(D) Example of a coronal section through A24b/M2 (bregma +0.50 mm) with cells labeled by rabies tracing from V1.

(E) Example images of A24b/M2 showing cells labeled by rabies tracing restricted to different starter cell populations in V1. PV, parvalbumin-positive interneurons; VIP, vasoactive intestinal peptide-positive interneurons; SST, somatostatin-positive interneurons; CR, calretinin-positive interneurons; Wfs1, expression mainly in layer 2/3; Scnn1a, expression mainly in layer 4; Rbp4, expression mainly in layer 5; Ntsr1, expression mainly in layer 6.

(F) Average number of labeled cells in A24b/M2 normalized by the number of starter cells in V1 for each Cre line.

See also Figure S1 and Movie S1.

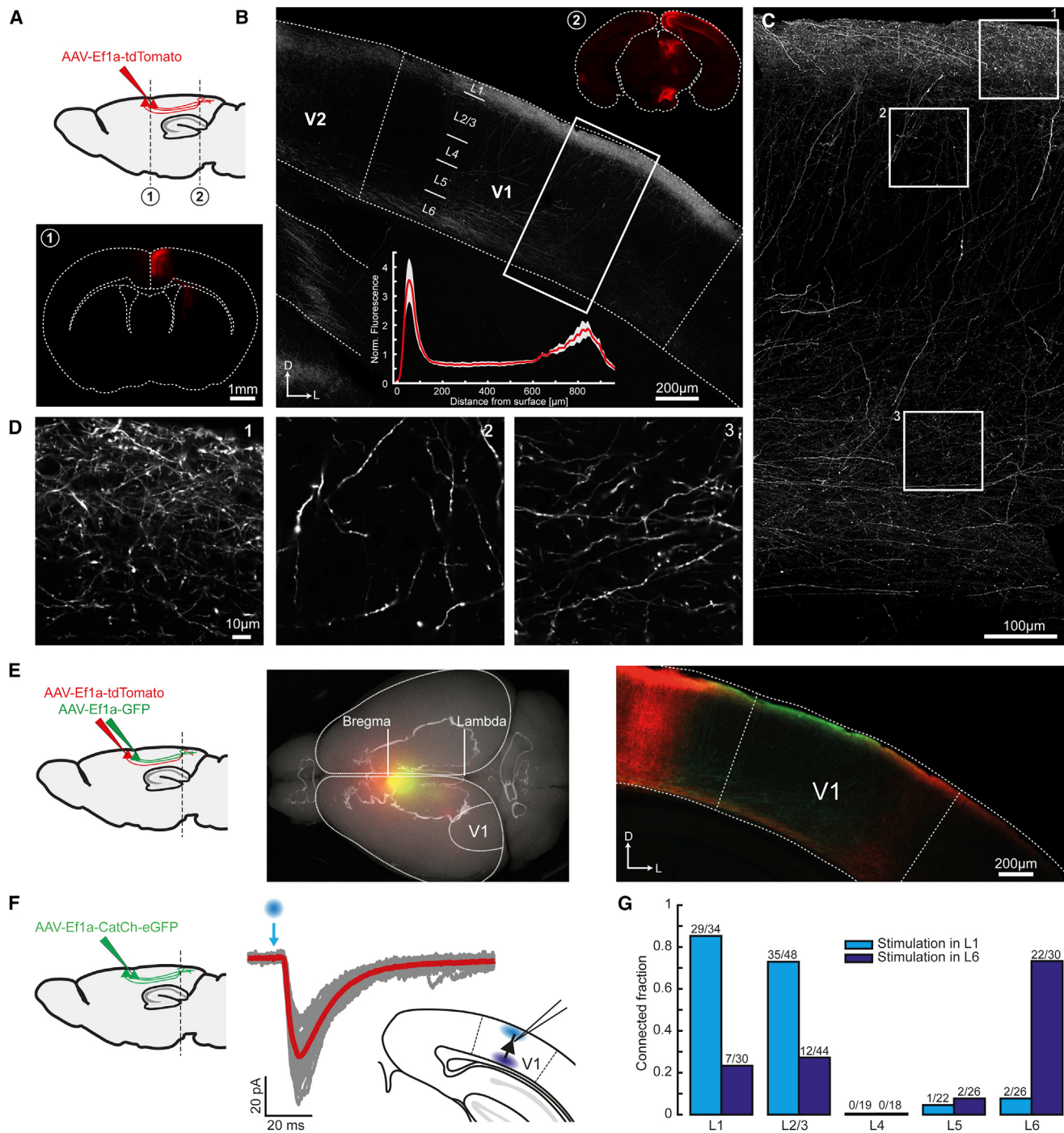


Figure 2. Axonal Input from A24b/M2 to V1 Is Dense and Maintains Topography

(A) Top: Injection scheme to label A24b/M2 axons in V1. Dashed lines indicate the locations of the coronal sections shown below and in (B). Bottom: Wide-field fluorescence image of a coronal section at the location of the injection site.

(B) Coronal section showing A24b/M2 axons in V1 and adjacent structures. A24b/M2 axons mainly innervate layer 1, 5, and 6 in V1. Box indicates magnified view shown in (C). Top inset: Wide-field fluorescence image of a coronal section of the whole brain at the location indicated in (A) (lambda +0.40 mm). A24b/M2 axons shown in red innervate V1, retrosplenial cortex, and subcortical structures. Bottom inset: Fluorescent labeling density as a function of depth from the surface of cortex in V1 (averaged over data from seven mice; shading indicates SEM).

(C) Maximum intensity projection of confocal images of the region marked in (B) showing dense innervation of V1 by A24b/M2 axons. Boxes correspond to the magnified views shown in (D).

(D) Confocal images of axons in layer 1 (1), layer 2/3 (2), and layer 6 (3).

(legend continued on next page)

and Paxinos, 2012), 57% (1,001 of 1,748) of the neurons were in A24b, and 43% (747 of 1,748) of the rabies-positive neurons were in M2. As we find no evidence of a separation between the population of neurons in A24b and the subset of neurons in the immediately adjacent medial part of M2, we refer to this region of cortex that projects to V1 as A24b/M2. Most of the presynaptically labeled cells in A24b/M2 were located in layer 5 (Figures 1D, S1A, and S1B). All further analysis was focused on A24b/M2 as a potential source of motor-related input to V1.

To identify the target cell types of the projection from A24b/M2 to V1, we performed a series of cell-type-specific rabies tracing experiments by restricting the expression of the TVA receptor and G protein to genetically defined populations of neurons. We injected AAV2/1-Ef1a-DIO-TVA950-T2A-CVS11G and EnvA-coated SADΔG into V1 of mice expressing Cre in different subpopulations of inhibitory neurons (parvalbumin [PV], vasoactive intestinal peptide [VIP], somatostatin [SST], or calretinin [CR]) or excitatory neurons predominantly in layer 2/3 (Wfs1-Cre), layer 4 (Scnn1a-Cre), layer 5 (Rbp4-Cre), or layer 6 (Ntsr1-Cre). We found that all tested neuron types in V1 receive input from A24b/M2 (Figures 1E and 1F). The largest fraction of presynaptically labeled cells in A24b/M2 was found when tracing from layer 2/3 and layer 6 excitatory neurons and PV interneurons.

Axonal Input from A24b/M2 to V1 Is Dense and Maintains Topography

To quantify the innervation pattern of A24b/M2 axons in V1, we labeled axons from A24b/M2 with a red fluorescent protein by injecting AAV2/1-Ef1a-tdTomato in A24b/M2 (Figure 2A). A24b/M2 axons densely innervate layer 1 and layer 6 of V1 (Figures 2B–2D). To test if there is a topographic structure to the projection, we injected two AAVs expressing either eGFP or tdTomato 500 μm apart into A24b/M2, separated along either the anterior-posterior (Figure 2E) or the medio-lateral axis (Figures S1C–S1E). We found that posterior A24b/M2 projects to medial V1, and anterior A24b/M2 projects to lateral V1. Conversely, medial A24b/M2 projects to anterior V1, and lateral A24b/M2 projects to posterior V1. Thus, the projection from A24b/M2 to V1 maintains topography.

To quantify the fraction of neurons in different layers of V1 that receive direct input from A24b/M2, we used channelrhodopsin-2-assisted circuit mapping (CRACM) (Petreanu et al., 2007). We expressed channelrhodopsin-2 in A24b/M2 neurons by injecting an AAV2/1-Ef1a-CatCh-eGFP into A24b/M2 and sacrificed mice 21 days later for slice recording experiments (see STAR Methods). We performed voltage-clamp recordings from neurons throughout all layers of V1 and recorded excitatory postsyn-

aptic currents (EPSCs) in response to optical stimulation of A24b/M2 axons in either layer 1 or layer 6 (Figure 2F). To ensure that the evoked EPSCs were monosynaptic, the stimulation intensity was set far below the threshold necessary to trigger action potentials in V1 neurons in current-clamp recordings (see STAR Methods). Depending on the site of stimulation, we found evoked responses in most neurons of layer 1 (29 of 34, or 85%), layer 2/3 (35 of 48, or 73%), and layer 6 (22 of 30, or 73%; Figure 2G). Only a small fraction of layer 5 neurons (2/26, or 8%) and no layer 4 neurons (0/19, or less than 5%) exhibited A24b/M2 axon photo-stimulation-evoked responses. On average the response latencies of the EPSCs were short (6.74 ± 3.27 ms, mean ± SD), consistent with a monosynaptic input (Figures S1F–S1H) (Petreanu et al., 2007). Thus, consistent with rabies tracing experiments, we found that A24b/M2 input mainly targets layers 1, 2/3, and 6 and directly innervates many of the neurons in these layers.

A24b/M2 Axons Convey Motor-Related Signals to V1

Activity in mouse V1 has been shown to reflect visual (Niell and Stryker, 2008), motor-related (Keller et al., 2012; Saleem et al., 2013), and visuomotor-mismatch signals (Keller et al., 2012; Saleem et al., 2013). To quantify a potential contribution of A24b/M2 input to these signals in V1, we transfected cells in A24b/M2 with an AAV2/1-Ef1a-GCaMP6f (Chen et al., 2013) and imaged activity of A24b/M2 axons in V1 (6,007 axons in ten mice) of head-fixed mice running on a spherical treadmill surrounded by a toroidal screen that provided visual flow feedback (Figure 3A) (Dombeck et al., 2007). Mice were exposed to either closed-loop conditions, in which visual flow feedback was coupled to locomotion and brief halts of visual flow were used to probe for mismatch responses; open-loop conditions, in which visual flow was presented independent of locomotion; or dark conditions (see STAR Methods). We found that the population of A24b/M2 axons exhibited strong motor-related activity that preceded running onsets by several hundred milliseconds (approximately 900 ms; see STAR Methods; Figure 3B). This anticipatory activity was stronger and started earlier than the anticipatory activity observed in layer 2/3 of visual cortex. To test whether the increased anticipatory activity was the result of a shift in the onset of activity in all axons or the result of the broadening of the distribution of onset times across the population of axons, we analyzed the distribution of the time differences between activity onset and running onset in the A24b/M2 axons and layer 2/3 V1 neurons. Although a substantial fraction of A24b/M2 axons (30%, 508 of 1,675) had activity onsets that preceded running onset, the average latency to activity onset followed the running onset (0.28 ± 0.13 s post-running onset,

(E) Left: Injection scheme for dual-color AAV topographic mapping. An AAV2/1-Ef1a-eGFP and an AAV2/1-Ef1a-tdTomato were injected separately, spaced by approximately 500 μm along the anterior-posterior axis in A24b/M2. The dashed line indicates the position of the coronal section shown on the right. Middle: Wide-field fluorescence image of the brain 3 weeks post-injection. Right: Pattern of labeling of A24b/M2 axons in V1. Anterior A24b/M2 (in red) projects to lateral V1 and posterior A24b/M2 (in green) projects to medial V1.

(F) Left: Injection scheme for CRACM. An AAV2/1-Ef1a-CatCh-eGFP was injected into A24b/M2. The dashed line indicates the position of coronal slices used for patch-clamp recordings. Middle: Example stimulation responses of a layer 2/3 neuron to stimulation of layer 1 axons (gray, single trials; red, average). Right: Recording scheme. Neurons were patched in different layers of V1 while axons were stimulated either in layer 1 or layer 6.

(G) Fraction of neurons with a significant response to A24b/M2 axon stimulation for each cortical layer, stimulated either in layer 1 or layer 6. Numbers above bars indicate the number of neurons with a significant response out of the total number of neurons recorded.

See also Figure S1.

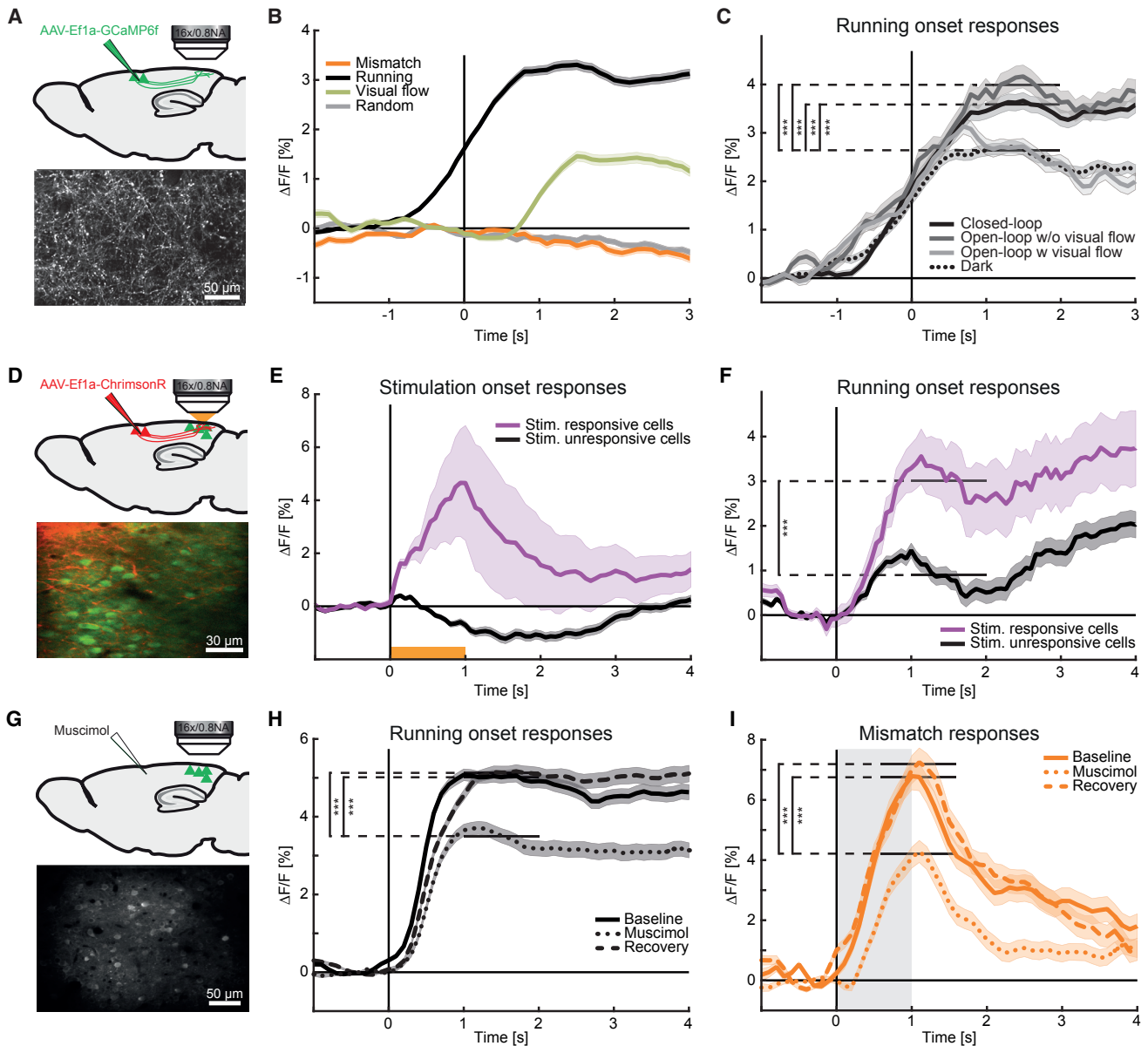


Figure 3. A24b/M2 Axons Convey Motor-Related Signals to V1

(A) Top: Schematic of axonal labeling and imaging. We injected an AAV-expressing GCaMP6f in A24b/M2 and recorded the activity of A24b/M2 axons in V1. Bottom: Example two-photon image of A24b/M2 axons in V1.

(B) Average population response of A24b/M2 axons (6,007 axons, 100 imaging sites, ten mice) in V1 to running onset (black line), visual flow onset (green line), mismatch onset (orange line), and triggered on random times (gray). Here and in the following panels, shading indicates SEM.

(C) Average population response of A24b/M2 axons in V1 to running onset during a closed-loop session (black line), during an open-loop session without visual flow prior to running onset (dark gray line) and with visual flow prior to running onset (light gray line), and during darkness (dotted black line). The visual stimulus preceding running onset strongly influences running onset activity in A24b/M2 axons (closed-loop versus open-loop with visual flow, $p = 1 \times 10^{-4}$; and versus dark, $p = 2 \times 10^{-6}$; open-loop without visual flow versus open-loop with visual flow, $p = 4 \times 10^{-8}$; and versus dark, $p = 2 \times 10^{-10}$; Student's t test, solid horizontal lines indicate testing window).

(D) Top: Schematic of simultaneous axonal stimulation and imaging. We expressed ChrismR-tdTomato in A24b/M2 neurons and stimulated the A24b/M2 axons in V1 while recording GCaMP6f activity of layer 2/3 neurons in V1. Bottom: Example two-photon image of A24b/M2 axons expressing ChrismR (shown in red) and layer 2/3 neurons expressing GCaMP6f (shown in green) in V1.

(E) We stimulated A24b/M2 axons in V1 of behaving mice while simultaneously recording the responses of V1 neurons. Eighty-two of 648 neurons (or 13%) in V1 exhibited significant responses to the stimulation of A24b/M2 axons (purple line). Stimulation duration is indicated by the orange bar (1 s, 20 Hz, 50% duty cycle).

(F) Running onset response of neurons selected in (E) that were strongly activated by A24b/M2 axon stimulation (purple line) and neurons that were not activated by A24b/M2 axon stimulation (black line; $p = 3 \times 10^{-5}$, Student's t test, solid horizontal lines indicate testing window).

(legend continued on next page)

ten mice, mean \pm SEM), but preceded the average latency to response in layer 2/3 V1 neurons (0.43 ± 0.06 s post-running onset, eight mice, mean \pm SEM). However, the main effect contributing to the stronger anticipatory activity in A24b/M2 axons was a broader distribution of activity-onset times (FWHM of the distribution of A24b/M2 axon response times: 1.08 ± 0.18 s; FWHM of the distribution of layer 2/3 V1 neuron response times: 0.52 ± 0.16 s; **Figure S2A**). Consistent with the idea that this motor-related activity is not just the consequence of a brain state change, we found that the amplitude of the motor-related activity in the A24b/M2 axons increased with increasing running speed (**Figure S2B**). In addition to motor-related signals, we also found responses to visual stimulation in open-loop conditions in A24b/M2 axons that occurred with a delay of approximately 1,000 ms after visual flow onset. We found no evidence of a correlation between the strength of an axon's response to visual flow onset and the strength of the axon's motor-related response (**Figure S2C**). Finally, we quantified the response of A24b/M2 axons to visuomotor mismatch, which results in strong mismatch responses in layer 2/3 neurons of V1 ([Keller et al., 2012](#)), and did not find any change in activity induced by mismatch (**Figure 3B**).

To test if motor-related activity in A24b/M2 axons depends on visual input prior to running onset, we analyzed activity in four different conditions: (1) running onset in the closed-loop condition, (2) running onset in the open-loop condition without visual flow preceding the running onset, (3) running onset in the open-loop condition with visual flow preceding running onset, and (4) running onset in darkness (**Figure 3C**; see **Figure S2D** for the same data before matching running speeds). We found that activity in A24b/M2 axons immediately following running onset depended strongly on visual flow preceding the running onset. Activity was highest when the mouse was seeing a static grating prior to the onset of running (conditions 1 and 2) and lower when the mouse either saw an already moving grating (condition 3) or nothing (darkness; condition 4) prior to running onset. The suppressive effect of visual flow was most pronounced when visual flow occurred in a 3 s window preceding running onset (**Figure S2E**). Consistent with a modulation of A24b/M2 responses by visual flow, A24b/M2 axons exhibited a marked decrease in activity when we switched to darkness while the mouse was running (**Figures S2F** and **S2G**). Hence, the motor-related activity in A24b/M2 axons is suppressed by either a lack of visual input or by visual flow preceding running onset.

To test if A24b/M2 axons specifically target neurons in layer 2/3 of V1 that exhibit strong motor-related activity, we developed an *in vivo* version of CRACM (ivCRACM). We injected an

AAV2/1-hSyn-ChrisonR-tdTomato into A24b/M2 and an AAV2/1-Ef1a-GCaMP6f into V1 (**Figure 3D**). To identify neurons driven by activity in A24b/M2 axons, we stimulated A24b/M2 axons locally in V1 and measured the calcium responses of layer 2/3 neurons (see [STAR Methods](#)). We identified 82 of 648 (or 13%) neurons that responded significantly to the local stimulation of A24b/M2 axons (**Figures 3E**, **S3A**, and **S3B**). Note that with this method we likely identify only those neurons in V1 that receive the strongest A24b/M2 input and not all neurons that are connected. Consistent with the idea that motor-related activity in A24b/M2 axons drives motor-related activity in V1, stimulation-responsive neurons also exhibited stronger motor-related activity than neurons that did not respond to A24b/M2 axon stimulation (**Figure 3F**). This was not simply the consequence of these neurons being more active than non-responsive neurons (**Figure S3C**). We also verified that the stimulation responses were absent in V1 neurons of control mice that did not express ChrisonR in A24b/M2 axons under otherwise identical conditions (**Figure S3D**). This demonstrates that A24b/M2 input best activates neurons in V1 with the highest running-onset activity.

To test if A24b/M2 suppression affects motor-related signals in V1, we inactivated A24b/M2 in a separate set of mice while recording neural activity in V1. We expressed GCaMP6f in V1 and recorded running onset and mismatch responses 1 day before, immediately after, and 1 day after muscimol injection into A24b/M2 (**Figure 3G**). We found that both running onset responses (**Figure 3H**) and mismatch responses (**Figure 3I**) were significantly decreased in responsive neurons during inactivation of A24b/M2 (see [STAR Methods](#)). This inactivation experiment has two confounding factors. First, inactivating A24b/M2 led to changes in motor behavior. On average, mice decreased average running speed during A24b/M2 inactivation (**Figure S2H**). To correct for a possible bias of differences in running speed, average running speed was matched across conditions by subsampling individual running onset and mismatch trials (see [STAR Methods](#); **Figures S2I** and **S2J**). Second, the inactivation volume likely encompassed only a fraction of the total A24b/M2 volume. Thus, the true effect size of a complete A24b/M2 inactivation is likely larger than the effects we report here. To rule out the possibility that the decrease in running onset responses and mismatch responses is the result of an acute off-target effect ([Otchy et al., 2015](#)), we also performed chronic lesions of A24b/M2 using ibotenic acid injections into A24b/M2. Consistent with the acute inactivation, both motor-related activity and mismatch responses were reduced following a chronic lesion of A24b/M2 (**Figures S2K** and **S2L**).

(G) Top: Schematic of A24b/M2 silencing during V1 imaging. We injected muscimol in A24b/M2 while recording GCaMP6f activity of layer 2/3 neurons in V1. Bottom: Example two-photon image of neurons in layer 2/3 of V1 expressing GCaMP6f.

(H) Average population response of running-onset-responsive neurons (50% most running-onset-responsive neurons selected on preceding time points; 1,934 of 3,868 neurons; see [STAR Methods](#)) in V1 to running onset before (baseline; solid line), during (muscimol; dotted), and after (recovery; dashed) inactivation of A24b/M2 (baseline versus muscimol: $p = 5 \times 10^{-9}$; recovery versus muscimol: $p = 3 \times 10^{-10}$; Student's t test, solid horizontal lines indicate testing window).

(I) Average population response of mismatch-responsive neurons (50% most mismatch-responsive neurons selected on preceding time points; 1,934 of 3,868 neurons; see [STAR Methods](#)) in V1 to mismatch before (baseline; solid line), during (muscimol; dotted), and after (recovery; dashed) inactivation of A24b/M2 (baseline versus muscimol: $p = 1 \times 10^{-10}$; recovery versus muscimol: $p = 1 \times 10^{-9}$; Student's t test, solid horizontal lines indicate testing window). Gray shading indicates the duration of feedback mismatch.

See also **Figures S2** and **S3**.

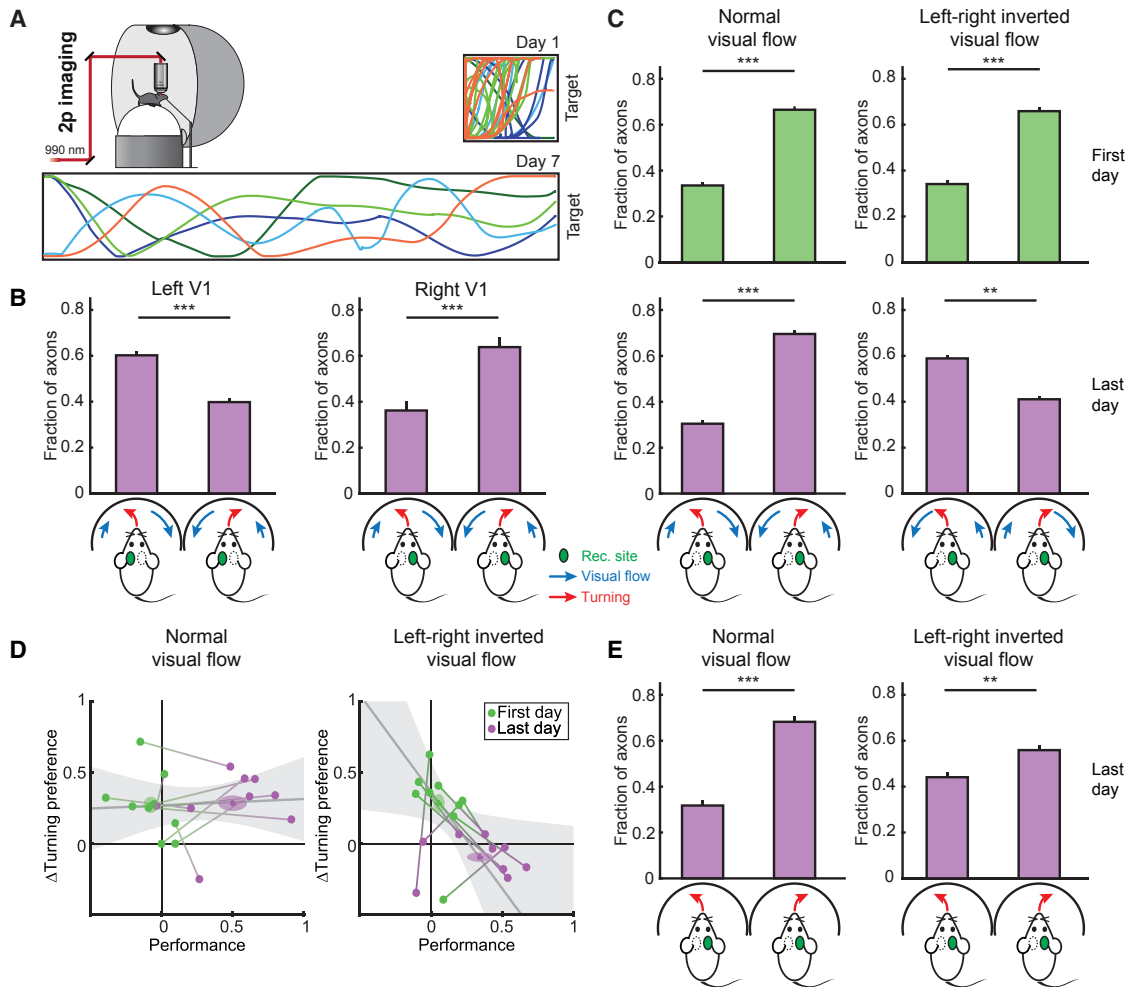


Figure 4. A24b/M2 Input Correlates with the Expected Visual Feedback Given a Motor Output

(A) Top left: Schematic of the virtual reality setup used to test mice in a 2D navigation task while imaging GCaMP6f-labeled A24b/M2 axons in V1. Top right: Five example trajectories of a mouse from the first training session on day 1. Bottom: Five example trajectories of a mouse from the last training session on day 7. Length of the tunnel is not shown to scale; the length/width ratio on day 1 was 5, and on day 7 it was 22. Length of the tunnel was increased as the mouse's performance increased.

(B) Fractions of axons that correlate best with a turn to the left or a turn to the right in either left or right monocular V1 ($22\% \pm 1.4\%$ mean \pm SEM of axons per recording site correlated with behavior, only these axons were included in the analysis shown here and in (C); left V1, $p = 4 \times 10^{-13}$, 16 sites in 8 mice; right V1, $p = 3 \times 10^{-5}$, 40 sites in 9 mice; Mann-Whitney U test). Note that activity in A24b/M2 axons in either hemisphere correlated best with the turn that maximizes visual flow in the corresponding retinotopic location. Activity was recorded during the last training session. Here and in the following panel, error bars indicate SEM, and in the schematic below, the red arrow indicates the turning behavior of the mouse, the blue arrows indicate the direction and magnitude of the resulting visual flow, and the green region marks the hemispheric location of V1 recordings.

(C) For mice trained with normal visual flow, activity in A24b/M2 axons in right V1 correlated best with right turns across learning (first day, $p = 9 \times 10^{-13}$, 47 sites in 9 mice; last day, $p = 2 \times 10^{-10}$, 37 sites in 6 mice; Mann-Whitney U test). In mice trained in a left-right inverted virtual reality, activity in most A24b/M2 axons in right V1 initially correlated best with right turns, but after learning activity in most A24b/M2 axons correlated best with left turns (first day, $p = 1 \times 10^{-10}$, 39 sites in 9 mice; last day, $p = 0.002$, 23 sites in 5 mice; Mann-Whitney U test). Note that left turns maximize visual flow on the left of the mouse in the left-right inverted virtual reality.

(D) Learning-related changes in the A24b/M2 axon turning preference as a function of behavioral performance. For both groups of mice (normal trained and left-right inverted trained), the difference between the fraction of axons best correlated with ipsiversive turns and the fraction of axons best correlated with contraversive turns (defined as the turning preference) was positive (more axons best correlated with ipsiversive turns) on the first day of training (green dots). This turning preference became increasingly negative (more axons best correlated with contraversive turns), with improved behavioral performance (last day, magenta dots) for mice trained in left-right inverted virtual reality, but not for normally trained mice. Each pair of dots corresponds to one mouse. Shaded ovals mark mean and SEM across mice. The gray line is a linear fit to the data (Deming regression), and the shading marks the 95% confidence interval of the fit.

(E) For both groups of mice (normal trained and left-right inverted trained), activity in A24b/M2 axons in right V1 correlated best with right turns after training in the absence of visual flow (normal trained animals, $p = 4 \times 10^{-4}$, 11 sites in 3 mice; left-right inverted animals, $p = 0.002$, 16 sites in 4 mice; Mann-Whitney U test). See also Figure S4 and Movie S2.

A24b/M2 Input to V1 Correlates with Expected Visual Feedback Given a Motor Output

To test if activity in A24b/M2 axons correlates with specific motor behaviors, we trained mice to navigate to the end of a 2D virtual tunnel and simultaneously recorded the activity of ipsilateral A24b/M2 axons in either the left or right monocular V1 (Figure 4A and Movie S2; left V1: 153 sites, 34,533 axons; right V1: 55 sites, 7,476 axons). On average we found that $22\% \pm 1.4\%$ (mean \pm SEM) of axons exhibited activity that was task-related (as defined by correlation with locomotion or rotation, see STAR Methods). These axons were then classified as correlating either with left turns or with right turns based on the correlation of their activity with the mouse's movement trajectory in the virtual environment (see STAR Methods). In left monocular V1, we found a bias for axons whose activity correlated with left turns (Figure 4B; left hemisphere: fraction 0.60 versus 0.40 ± 0.02 , $p = 4 \times 10^{-13}$, Mann-Whitney U test, $60\% \pm 5\%$ of axons). Conversely, in right monocular V1 we found a bias for axons whose activity correlated with right turns (Figure 4B; right hemisphere: 0.36 versus 0.64 ± 0.04 , $p = 2 \times 10^{-5}$, Mann-Whitney U test, $58\% \pm 10\%$ of axons). There are two possible interpretations of these observations. One is that A24b/M2 axons innervating a particular part of V1 are activated more strongly by the movements that increase visual flow in the corresponding area of visual space. The other is that this hemispheric bias is a consequence of a general bias of neural activity to the laterality of the movement, which has been described in motor cortex (Li et al., 2015) and the striatum (Cui et al., 2013). To distinguish between these alternatives, we tested if this bias in activity of A24b/M2 axons depends on visuomotor experience. We trained a different group of mice to perform navigation in left-right inverted virtual reality until they reached a certain performance criterion (up to 10 sessions, 1 session per day, see STAR Methods). Mice learned to perform this task despite left-right inversion, albeit more slowly than under normal conditions (Figure S4A). We recorded activity of A24b/M2 axons in right monocular V1 on the first and on the last training day. On the first day, we found a bias for axons whose activity correlated with ipsiversive turns, similar to the bias observed in mice trained in the non-inverted environment (Figure 4C). However, after mice learned to navigate the left-right inverted virtual environment, we found an inverse bias of the activity of A24b/M2 axons; most of the task-related axons in right V1 correlated best with a contraversive turn, which under left-right inversion maximizes visual flow in the left visual field. This shift in preference for contraversive turns was larger in mice with higher performance in the left-right inverted environment (Figure 4D). To test whether the shift in preference was specific to the navigation task in which visual feedback is coupled to the mouse's movement, or is simply a reversal in the preference of the motor-related or the visually driven activity, we exposed a subset of the mice to both a no-visual flow condition and to an independent visual flow condition before and after training. In the no-visual flow condition, the walls of the corridor in the virtual environment were uniformly gray, but the mouse was free to run on the spherical treadmill. When measured in the absence of visual flow coupled to the movement of the mouse, we found no reversal of the preference in mice trained either under normal conditions or under left-right inverted conditions (Figure 4E).

Similarly, when measured in the independent visual flow condition, which consisted of the mouse watching a playback of visual flow, the preference of A24b/M2 axons for either ipsi- or contraversive visual flow equalized but did not revert in mice trained under left-right inverted conditions and was unchanged in mice trained under normal conditions after training (Figure S4B). Hence, the reversal of preference is strongest in conditions in which visual flow is coupled to movement. In sum, activity in A24b/M2 axons in a particular retinotopic location in V1 is dynamically adapted to changes in visuomotor coupling with learning in such a way that A24b/M2 axons are activated most strongly by movements that maximize visual flow in the corresponding part of the visual space.

Finally, to test if artificial activation of A24b/M2 axons in V1 could affect the behavior of the mouse, we expressed channelrhodopsin-2 in A24b/M2 by injecting an AAV2/1-Ef1a-CatCh-eGFP into both left and right A24b/M2 and trained mice to navigate the virtual tunnel. On the seventh day of training, we briefly stimulated axons (3 s at 25 Hz; see STAR Methods) in left, right, or both left and right monocular V1 as mice were navigating to the end of the tunnel. To control for unspecific effects of the stimulation on behavior, we compared the stimulation of left or right V1 to a bilateral stimulation of both left and right V1, as A24b/M2 axon stimulation always led to a marked decrease in running speed (Figures S4C and S4D). In response to stimulation of A24b/M2 axons in left V1, mice turned to the right. Vice versa, in response to the stimulation of A24b/M2 axons in right V1, mice turned to the left (Figure 5). In summary, artificial activation of A24b/M2 axons in either left or right monocular V1 resulted in a behavioral response consistent with the bias in their activity we observed during voluntary turning behavior (Figure 4).

DISCUSSION

Cortical function can be described in a representation framework that is based on the notion of the feature detector (Barlow, 1953; Marr, 1982) or in a predictive processing framework (Clark, 2013; Friston, 2005; Hawkins and Blakeslee, 2004). The predictive processing framework postulates that feedforward sensory signals are compared against a top-down prediction of sensory feedback to detect prediction errors. Evidence for the predictive processing framework has come from, among other things, the discovery of sensorimotor mismatch signals in sensory areas of cortex (Attänger et al., 2017; Eliades and Wang, 2008; Keller and Hahnloser, 2009; Keller et al., 2012; Zmarz and Keller, 2016) that could constitute prediction errors. Mismatch signals in mouse visual cortex are the result of a comparison of an excitatory motor-related prediction and an inhibitory visual input (Attänger et al., 2017). A missing piece of the puzzle has been evidence for top-down predictions of sensory input given a movement. We now show that A24b/M2 provides a strong and dense projection to V1, which conveys motor-related signals that depend on the mouse's visuomotor experience. We suggest that these signals constitute a prediction of visual flow that is linked to the mouse's movement, consistent with an interpretation of the function of visual cortex in a predictive coding framework. This is detailed in the following:

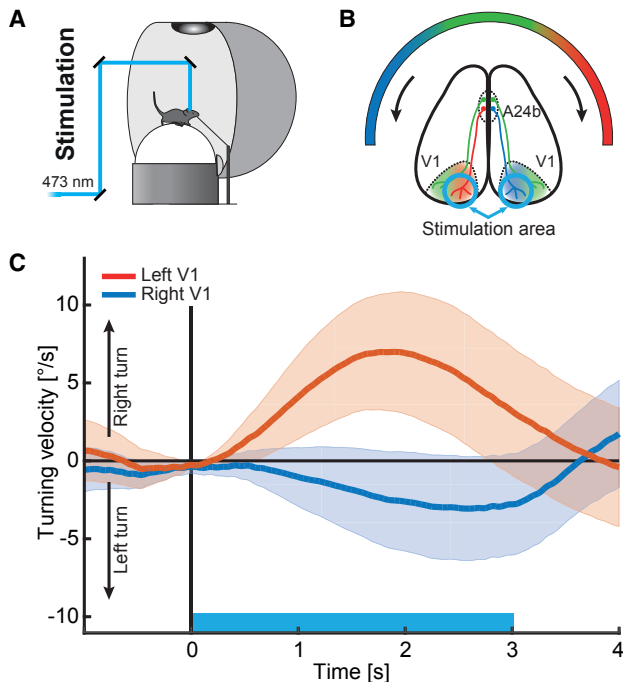


Figure 5. Artificial Stimulation of A24b/M2 Axons in Monocular V1 Causes Turning Behavior

(A) Schematic of the virtual reality setup used for stimulation experiments.
(B) Schematic top-down view of a mouse brain and the virtual reality screen illustrating the retinotopic mapping of the virtual reality onto V1 as well as the topographic mapping of axons from A24b/M2 to V1. Blue circles indicate areas stimulated with laser. Arrows indicate the direction of visual flow generated during forward locomotion.
(C) Average turning velocity (seven mice) induced by stimulation of A24b/M2 axons in left (red) or right (blue) V1. Stimulation of the A24b/M2 axons in right (left) monocular V1 in mice navigating toward a target resulted in turning to the left (right). Shading indicates SEM. Blue bar indicates stimulation period. See also Figure S4.

1. A motor-based prediction of visual flow in V1 requires an anatomical basis in the form of either a direct or an indirect projection from a motor-related area of the brain. We found that one of the largest inputs to V1 originates in A24b/M2 (Figure 1C), a motor-related area of cortex (Sinnamon and Galer, 1984).
2. Visuomotor mismatch signals have been reported in layer 2/3 neurons of V1 (Keller et al., 2012; Saleem et al., 2013). These mismatch signals can be explained by a difference between an excitatory prediction of visual flow and an inhibitory visual signal (Attinger et al., 2017; Zmarz and Keller, 2016). We found that layer 2/3 excitatory neurons are one of the main targets of the projection from A24b/M2 (Figures 1E and 1F).
3. Movements lead to visual feedback that systematically changes with retinotopic location. Moving head or eye to the left leads to full-field visual flow to the right. Moving forward, however, leads to radially symmetric visual flow of opposite direction in the left and right visual field. Thus, to simplify wiring, one would expect a certain amount of

conservation of topography in the process of a conversion from a myotopic coordinate system to a retinotopic coordinate system. We find that the projection from A24b/M2 to V1 coarsely maintains topography (Figure 2E).

4. To convey a prediction of visual input, the bandwidth of the projection would need to be roughly equivalent to the feedforward visual input from the dorsolateral geniculate nucleus (dLGN). The number of neurons in A24b/M2 providing input to V1 was roughly twice as large as that in dLGN (Figure 1C). In addition, we found that the projection from A24b/M2 to V1 is dense in that it targets more than 73% of all neurons in layers 1, 2/3, and 6 (Figures 2F and 2G).
5. Motor-related predictions of visual input should occur mainly during movements that elicit visual feedback and should not be activated by visuomotor mismatch. We found that A24b/M2 axons in V1 are strongly activated during locomotion and that activity precedes the onset of locomotion, but these axons remain silent during mismatch (Figure 3B).
6. The amplitude of the predictive signal should correlate with the magnitude of the predicted change in visual flow given the current visual stimulus. We found that running onset activity in A24b/M2 axons was significantly reduced if the running onset occurred either during darkness or during open-loop conditions with visual flow preceding running onset (Figure 3C). In both cases, the predicted change in visual flow resulting from a running onset is lower, either due to a lack of visual information or due to ongoing visual flow prior to the running onset.
7. An inhibition of an excitatory predictive signal should result in a reduction of both motor-related activity and mismatch signals in V1 neurons that respond strongly to running or mismatch. We found that inhibition of A24b/M2 reduces both motor-related and mismatch signals in running and mismatch-responsive V1 neurons (Figures 3H and 3I).
8. If predictions are transmitted in visual coordinates, they should be stronger in a given retinotopic location in V1 for behaviors that maximize visual flow in the corresponding part of the visual field. We found that activity in A24b/M2 axons in monocular V1 correlated better with ipsiversive turns, which maximize visual flow in the contralateral visual field (Figure 4B).
9. A key premise of predictive coding theories is that predictions are continuously updated based on prediction errors. Thus, if there are changes in the way visual feedback is coupled to motor output, predictions of visual feedback should adapt to reflect the new form of visuomotor coupling. We found that in mice trained in left-right inverted visual environment, activity of A24b/M2 axons in right V1 correlated better with left turns, consistent with the fact that in this left-right inverted virtual environment, left turns maximize visual flow in the left visual field (Figure 4C). This change was larger in mice that had a higher performance in left-right inverted navigation (Figure 4D).

and was smaller for both correlation with running and visual flow separately (Figures 4E and S4B).

10. Artificial stimulation of a projection that conveys a prediction of visual flow in a particular retinotopic location in V1 should result in illusory visual flow in the corresponding part of the visual field. We found that stimulating A24b/M2 axons in either right or left monocular V1 resulted in a corrective behavior of the mouse consistent with an adaptation to an illusory visual flow (Figure 5C).

While many of the individual findings have alternate interpretations, the interpretation of the signals as a prediction of visual flow provides a unified explanation of all our findings. Other explanations likely raise more questions than they answer. For example, the finding that stimulation of A24b/M2 axons results in a turning behavior could be explained by assuming that activity in A24b/M2 directly drives movement. However, this would not explain why neurons in A24b/M2 that directly drive movement would send collaterals to V1. Another concern with the interpretation of the signals as predictions of visual feedback may stem from the fact that activity in A24b/M2 axons in V1 is not absent in darkness. Here one should consider that V1 layer 2/3 neurons also exhibit motor-related activity in complete darkness (Keller et al., 2012; Saleem et al., 2013) that is persistent even under complete retinal lesions (Keck et al., 2013). This motor-related activity cannot, strictly speaking, be explained in either the representation framework or the predictive processing framework. In complete absence of visual input, there is no visually driven activity, and movement does not result in a predictable visual flow. However, in low light conditions, visual processing may increasingly rely on predictions with decreasing strength of visual signals, and complete darkness may be a singularity for which the system has not evolved to produce optimal predictions.

The projection from A24b/M2 to V1 fulfills all the criteria to be a top-down signal that conveys a motor-related prediction of visual flow in visual coordinates. Nevertheless, it is likely that the same projection also has other functions. For example, it has been shown to be involved in surround suppression of visual responses (Zhang et al., 2014), and we have recently shown that it also conveys a prediction of visual input based on spatial location of the mouse (Fiser et al., 2016). Moreover, given that there are also delayed visual responses in A24b/M2 axons in V1 (Figure 3B), our data are consistent with a model in which A24b/M2 conveys a general prediction of visual input given recent experience. It is also likely that A24b/M2 is not the only source of predictive input to V1. Similar predictions could be conveyed by all top-down inputs to V1. Inputs from secondary visual areas, for example, can be described in a predictive coding framework with respect to higher-level visual features (Rao and Ballard, 1999). We speculate that top-down input could in general be interpreted as a prediction of feedforward input. In this way, input to V1 from auditory cortex, for example, would provide a prediction of visual input given a learned association between a sound and a visual stimulus, while input from retrosplenial cortex, known to be activated by vestibular signals (Rancz et al., 2015), might provide a prediction of visual input based on a head or body rotation. Consistent with this, we find that A24b/M2 inactivation and lesion only result in a partial reduction of

motor-related and mismatch signals in V1. Note that in the framework of predictive coding, classically visual phenomena like attention and adaptation would also find a mechanistic interpretation (Feldman and Friston, 2010; Keller et al., 2017).

It is unclear how these findings of a projection from A24b/M2 to V1 extend to primate anatomy. A24b is likely homologous to primate A24b (Vogt and Paxinos, 2014; Vogt et al., 1987), but a connection from A24b to V1 similar to the one described in rodents (Miller and Vogt, 1984; Vogt and Miller, 1983) has not been described in primates (Vogt et al., 1979). However, using classical neural tracing methods, the projection from ACC to V1 in rats was estimated to be much weaker (Miller and Vogt, 1984; Vogt and Miller, 1983) than what we have found using rabies tracing in the mouse. This means either that classical tracing underestimates long-range cortical projections or that communication between ACC and visual cortex occurs primarily indirectly in rats and primates. In the human cortex, there is some evidence of functional connectivity between ACC and primary and secondary visual cortices (Zhou et al., 2016).

Predictive coding is a theoretical framework that describes the function of sensory processing in general and visual cortex in particular. Evidence for predictive coding has mainly come from theoretical considerations (Rao and Ballard, 1999; Spratling, 2010) and the discovery of mismatch signals in primary sensory areas of cortex and avian pallium (Eliades and Wang, 2008; Fiser et al., 2016; Keller and Hahnloser, 2009; Keller et al., 2012). One of the key pieces of evidence lacking for a description of cortical function in a framework of predictive coding is predictive top-down input. We have demonstrated here that the input from A24b/M2 to V1 fulfills all the criteria necessary to be interpreted as a prediction of visual flow given a motor output. Our data are consistent with a theory of predictive coding where the function of cortex is to generate and maintain an internal model of the world (Craik, 1943) by continuously updating and comparing this model to actual sensory input.

STAR METHODS

Detailed methods are provided in the online version of this paper and include the following:

- KEY RESOURCES TABLE
- CONTACT FOR REAGENT AND RESOURCE SHARING
- EXPERIMENTAL MODEL AND SUBJECT DETAILS
 - Animals and surgery
- METHOD DETAILS
 - Surgery
 - Rabies tracing
 - AAV tracing
 - CRACM
 - Axonal imaging
 - In vivo channelrhodopsin-2-assisted circuit mapping (ivCRACM)
 - Muscimol or ibotenic acid silencing of A24b
 - Virtual reality and navigation task
- QUANTIFICATION AND STATISTICAL ANALYSIS
 - Data analysis
- DATA AND SOFTWARE AVAILABILITY

SUPPLEMENTAL INFORMATION

Supplemental Information includes four figures and two movies and can be found with this article online at <http://dx.doi.org/10.1016/j.neuron.2017.08.036>.

AUTHOR CONTRIBUTIONS

M.L. designed the experiments and performed the imaging experiments. M.L. and J.M.S. performed the rabies and AAV tracing experiments. D.R.W. performed the CRACM experiments. A.A. developed ivCRACM, and M.L. and A.A. performed the ivCRACM experiments. M.L. performed all calcium imaging experiments and all analysis. M.L., A.A., and G.B.K. wrote the manuscript.

ACKNOWLEDGMENTS

We thank Thomas Mrsic-Flogel and Rainer Friedrich for comments on earlier versions of this manuscript. We thank Botond Roska and Keisuke Yonehara for invaluable help with the rabies virus production and Silvia Arber, Andreas Lüthi, and Botond Roska for generously providing mouse lines. We thank Daniela Gerosa-Ernri for production of the AAV vectors, Hassana Oyibo for production of the rabies virus, and all the members of the Keller lab for discussion, support, and comments on the manuscripts. This work was supported by the Swiss National Science Foundation, the Novartis Research Foundation, and the Human Frontier Science Program.

Received: October 28, 2016

Revised: June 30, 2017

Accepted: August 24, 2017

Published: September 13, 2017; corrected online: November 10, 2017

REFERENCES

- Attinger, A., Wang, B., and Keller, G.B. (2017). Visuomotor Coupling Shapes the Functional Development of Mouse Visual Cortex. *Cell* 169, 1291–1302.e14.
- Ayaz, A., Saleem, A.B., Schölvinck, M.L., and Carandini, M. (2013). Locomotion controls spatial integration in mouse visual cortex. *Curr. Biol.* 23, 890–894.
- Barlow, H.B. (1953). Summation and inhibition in the frog's retina. *J. Physiol.* 119, 69–88.
- Barlow, H.B. (1994). What is the computational goal of the neocortex? In Large-Scale Neuronal Theories of the Brain, C. Koch and J.L. Davis, eds. (MIT Press), pp. 1–22.
- Blakemore, S.J., Wolpert, D., and Frith, C. (2000). Why can't you tickle yourself? *Neuroreport* 11, R11–R16.
- Chen, T.-W., Wardill, T.J., Sun, Y., Pulver, S.R., Renninger, S.L., Baohan, A., Schreiter, E.R., Kerr, R.A., Orger, M.B., Jayaraman, V., et al. (2013). Ultrasensitive fluorescent proteins for imaging neuronal activity. *Nature* 499, 295–300.
- Clark, A. (2013). Whatever next? Predictive brains, situated agents, and the future of cognitive science. *Behav. Brain Sci.* 36, 181–204.
- Craik, K.J. (1943). The Nature of Explanation (Cambridge University Press London).
- Cui, G., Jun, S.B., Jin, X., Pham, M.D., Vogel, S.S., Lovinger, D.M., and Costa, R.M. (2013). Concurrent activation of striatal direct and indirect pathways during action initiation. *Nature* 494, 238–242.
- Dombeck, D.A., Khabbaz, A.N., Collman, F., Adelman, T.L., and Tank, D.W. (2007). Imaging large-scale neural activity with cellular resolution in awake, mobile mice. *Neuron* 56, 43–57.
- Eliades, S.J., and Wang, X. (2008). Neural substrates of vocalization feedback monitoring in primate auditory cortex. *Nature* 453, 1102–1106.
- Feldman, H., and Friston, K.J. (2010). Attention, uncertainty, and free-energy. *Front. Hum. Neurosci.* 4, 215.
- Felleman, D.J., and Van Essen, D.C. (1991). Distributed hierarchical processing in the primate cerebral cortex. *Cereb. Cortex* 1, 1–47.
- Fiser, A., Mahringer, D., Oyibo, H.K., Petersen, A.V., Leinweber, M., and Keller, G.B. (2016). Experience-dependent spatial expectations in mouse visual cortex. *Nat. Neurosci.* 19, 1658–1664.
- Franklin, K.B.J., and Paxinos, G. (2012). Paxinos and Franklin's The Mouse Brain in Stereotaxic Coordinates (Academic Press).
- Friston, K. (2005). A theory of cortical responses. *Philos. Trans. R. Soc. Lond. B Biol. Sci.* 360, 815–836.
- Friston, K. (2010). The free-energy principle: a unified brain theory? *Nat. Rev. Neurosci.* 11, 127–138.
- Fu, Y., Tucciarone, J.M., Espinosa, J.S., Sheng, N., Darcy, D.P., Nicoll, R.A., Huang, Z.J., and Stryker, M.P. (2014). A cortical circuit for gain control by behavioral state. *Cell* 156, 1139–1152.
- Gilbert, C.D., and Li, W. (2013). Top-down influences on visual processing. *Nat. Rev. Neurosci.* 14, 350–363.
- Gilbert, C.D., and Sigman, M. (2007). Brain states: top-down influences in sensory processing. *Neuron* 54, 677–696.
- Grosof, D.H., Shapley, R.M., and Hawken, M.J. (1993). Macaque V1 neurons can signal 'illusory' contours. *Nature* 365, 550–552.
- Hawkins, J., and Blakeslee, S. (2004). On intelligence (Times Books).
- Jordan, M.I., and Rumelhart, D.E. (1992). Forward Models: Supervised Learning with a Distal Teacher. *Cogn. Sci.* 16, 307–354.
- Keck, T., Keller, G.B., Jacobsen, R.I., Eysel, U.T., Bonhoeffer, T., and Hübener, M. (2013). Synaptic scaling and homeostatic plasticity in the mouse visual cortex in vivo. *Neuron* 80, 327–334.
- Keller, G.B., and Hahnloser, R.H.R. (2009). Neural processing of auditory feedback during vocal practice in a songbird. *Nature* 457, 187–190.
- Keller, G.B., Bonhoeffer, T., and Hübener, M. (2012). Sensorimotor mismatch signals in primary visual cortex of the behaving mouse. *Neuron* 74, 809–815.
- Keller, A.J., Houlton, R., Kampa, B.M., Lesica, N.A., Mrsic-Flogel, T.D., Keller, G.B., and Helmchen, F. (2017). Stimulus relevance modulates contrast adaptation in visual cortex. *eLife* 6, e21589.
- Leinweber, M., Zmarz, P., Buchmann, P., Argast, P., Hübener, M., Bonhoeffer, T., and Keller, G.B. (2014). Two-photon calcium imaging in mice navigating a virtual reality environment. *J. Vis. Exp.* e50885.
- Li, N., Chen, T.-W., Guo, Z.V., Gerfen, C.R., and Svoboda, K. (2015). A motor cortex circuit for motor planning and movement. *Nature* 519, 51–56.
- Marr, D. (1982). Vision (MIT Press).
- Miller, M.W., and Vogt, B.A. (1984). Direct connections of rat visual cortex with sensory, motor, and association cortices. *J. Comp. Neurol.* 226, 184–202.
- Mukamel, E.A., Nimmerjahn, A., and Schnitzer, M.J. (2009). Automated analysis of cellular signals from large-scale calcium imaging data. *Neuron* 63, 747–760.
- Niell, C.M., and Stryker, M.P. (2008). Highly selective receptive fields in mouse visual cortex. *J. Neurosci.* 28, 7520–7536.
- Niell, C.M., and Stryker, M.P. (2010). Modulation of visual responses by behavioral state in mouse visual cortex. *Neuron* 65, 472–479.
- Otchy, T.M., Wolff, S.B.E., Rhee, J.Y., Pehlevan, C., Kawai, R., Kempf, A., Gobes, S.M.H., and Ölveczky, B.P. (2015). Acute off-target effects of neural circuit manipulations. *Nature* 528, 358–363.
- Pakan, J.M., Lowe, S.C., Dylda, E., Keemink, S.W., Currie, S.P., Coutts, C.A., and Rochelefort, N.L. (2016). Behavioral-state modulation of inhibition is context-dependent and cell type specific in mouse visual cortex. *eLife* 5, e14985.
- Petreanu, L., Huber, D., Sobczyk, A., and Svoboda, K. (2007). Channelrhodopsin-2-assisted circuit mapping of long-range callosal projections. *Nat. Neurosci.* 10, 663–668.
- Polack, P.-O., Friedman, J., and Golshani, P. (2013). Cellular mechanisms of brain state-dependent gain modulation in visual cortex. *Nat. Neurosci.* 16, 1331–1339.

- Rancz, E.A., Moya, J., Drawitsch, F., Brichta, A.M., Canals, S., and Margrie, T.W. (2015). Widespread vestibular activation of the rodent cortex. *J. Neurosci.* 35, 5926–5934.
- Rao, R.P., and Ballard, D.H. (1999). Predictive coding in the visual cortex: a functional interpretation of some extra-classical receptive-field effects. *Nat. Neurosci.* 2, 79–87.
- Riesenhuber, M., and Poggio, T. (1999). Hierarchical models of object recognition in cortex. *Nat. Neurosci.* 2, 1019–1025.
- Roelfsema, P.R., Lamme, V.A., and Spekreijse, H. (1998). Object-based attention in the primary visual cortex of the macaque monkey. *Nature* 395, 376–381.
- Saleem, A.B., Ayaz, A., Jeffery, K.J., Harris, K.D., and Carandini, M. (2013). Integration of visual motion and locomotion in mouse visual cortex. *Nat. Neurosci.* 16, 1864–1869.
- Sinnamon, H.M., and Galer, B.S. (1984). Head movements elicited by electrical stimulation of the anteromedial cortex of the rat. *Physiol. Behav.* 33, 185–190.
- Spratling, M.W. (2010). Predictive coding as a model of response properties in cortical area V1. *J. Neurosci.* 30, 3531–3543.
- Vogt, B.A., and Miller, M.W. (1983). Cortical connections between rat cingulate cortex and visual, motor, and postsubiculum cortices. *J. Comp. Neurol.* 216, 192–210.
- Vogt, B.A., and Paxinos, G. (2014). Cytoarchitecture of mouse and rat cingulate cortex with human homologies. *Brain Struct. Funct.* 219, 185–192.
- Vogt, B.A., Rosene, D.L., and Pandya, D.N. (1979). Thalamic and cortical afferents differentiate anterior from posterior cingulate cortex in the monkey. *Science* 204, 205–207.
- Vogt, B.A., Pandya, D.N., and Rosene, D.L. (1987). Cingulate cortex of the rhesus monkey: I. Cytoarchitecture and thalamic afferents. *J. Comp. Neurol.* 262, 256–270.
- von Holst, E., and Mittelstaedt, H. (1950). Das Reafferenzprinzip. *Naturwissenschaften* 37, 464–476.
- Wertz, A., Trenholm, S., Yonehara, K., Hillier, D., Raics, Z., Leinweber, M., Szalay, G., Ghanem, A., Keller, G., Rózsa, B., et al. (2015). PRESYNAPTIC NETWORKS. Single-cell-initiated monosynaptic tracing reveals layer-specific cortical network modules. *Science* 349, 70–74.
- Wickersham, I.R., Lyon, D.C., Barnard, R.J.O., Mori, T., Finke, S., Conzelmann, K.-K., Young, J.A.T., and Callaway, E.M. (2007). Monosynaptic restriction of transsynaptic tracing from single, genetically targeted neurons. *Neuron* 53, 639–647.
- Wickersham, I.R., Sullivan, H.A., and Seung, H.S. (2010). Production of glycoprotein-deleted rabies viruses for monosynaptic tracing and high-level gene expression in neurons. *Nat. Protoc.* 5, 595–606.
- Wolpert, D., Ghahramani, Z., and Jordan, M. (1995). An internal model for sensorimotor integration. *Science* 269, 1880–1882.
- Zhang, S., Xu, M., Kamigaki, T., Hoang Do, J.P., Chang, W.-C., Jenvay, S., Miyamichi, K., Luo, L., and Dan, Y. (2014). Selective attention. Long-range and local circuits for top-down modulation of visual cortex processing. *Science* 345, 660–665.
- Zhang, S., Xu, M., Chang, W.-C., Ma, C., Hoang Do, J.P., Jeong, D., Lei, T., Fan, J.L., and Dan, Y. (2016). Organization of long-range inputs and outputs of frontal cortex for top-down control. *Nat. Neurosci.* 19, 1733–1742.
- Zhou, Y., Shi, L., Cui, X., Wang, S., and Luo, X. (2016). Functional Connectivity of the Caudal Anterior Cingulate Cortex Is Decreased in Autism. *PLoS ONE* 11, e0151879.
- Zipser, K., Lamme, V.A., and Schiller, P.H. (1996). Contextual modulation in primary visual cortex. *J. Neurosci.* 16, 7376–7389.
- Zmarz, P., and Keller, G.B. (2016). Mismatch Receptive Fields in Mouse Visual Cortex. *Neuron* 92, 766–772.

STAR★METHODS**KEY RESOURCES TABLE**

REAGENT or RESOURCE	SOURCE	IDENTIFIER
Antibodies		
Chicken Anti-GFP	Abcam	RRID: AB_300798
Anti-2A Peptide	Millipore	RRID: AB_11214282
Anti-NeuN	Millipore	RRID: AB_2298772
Alexa Fluor 488 Donkey Anti-Chicken IgY	Jackson ImmunoResearch	RRID: AB_2340375
Alexa Fluor 568 donkey anti - rabbit IgG	ThermoFisher	RRID: AB_2534017
Alexa Fluor 647 donkey anti - mouse IgG	ThermoFisher	RRID: AB_162542
Bacterial and Virus Strains		
AAV2/1-EF1a-GCaMP6f-WPRE	FMI Vector Core	N/A
AAV2/1-Ef1a -TVA950-T2A-CVS11G	FMI Vector Core	N/A
AAV2/1-Ef1a -DIO-TVA950-T2A-CVS11G	FMI Vector Core	N/A
EnvA-SADΔG-GCaMP6s	FMI Vector Core	N/A
AAV2/1-Ef1a-tdTomato-WPRE	FMI Vector Core	N/A
AAV2/1-Ef1a-eGFP-WPRE	FMI Vector Core	N/A
AAV2/1-Ef1a-CatCh-eGFP	FMI Vector Core	N/A
AAV2/1-Ef1a-DIO-eGFP	FMI Vector Core	N/A
AAV2/1-hSyn-ChrimsonR-tdTomato-WPRE	FMI Vector Core	N/A
Chemicals, Peptides, and Recombinant Proteins		
Isoflurane (Attane)	Provet	CAS 26221-73-3
Fentanyl	Actavis	CAS 990-73-8
Midazolam (Dormicum)	Roche	CAS 59467-96-8
Medetomidine (Dormitor)	Orion	CAS 86347-14-0
Flumazenil (Anexate)	Roche	CAS 78755-81-4
Atipamezole (Antisedan)	Orion Pharma	CAS 104054-27-5
Histoacryl	B. Braun	CAS 6606-65-1
Dental cement (Paladur)	Heraeus Kulzer	CAS 9066-86-8
Tamoxifen	Sigma-Aldrich	CAS 10540-29-1
Muscimol	Sigma-Aldrich	CAS 2763-96-4
Ibotenic acid	Abcam	CAS 2552-55-8
Experimental Models: Organisms/Strains		
Mouse: C57BL6/J	Charles River Laboratories	N/A
Mouse: Pvalb ^{tm1(cre)Arb}	The Jackson Laboratory	RRID: IMSR_JAX:008069
Mouse: Sst ^{tm2.1(cre)Zjh}	The Jackson Laboratory	RRID: IMSR_JAX:018973
Mouse: Vip ^{tm1(cre)Zjh}	The Jackson Laboratory	RRID: IMSR_JAX:010908
Mouse: CR ^{tm1(cre)Zjh}	The Jackson Laboratory	RRID: IMSR_JAX:010774
Mouse: Wfs1-Tg2-CreERT2	The Jackson Laboratory	RRID: IMSR_JAX:009103
Mouse: Scnn1a-Tg3-Cre	The Jackson Laboratory	RRID: IMSR_JAX:009613
Mouse: Rbp4 ^{KL100Gsat/Mmucl}	MMRRC	RRID: MMRRC_031125-UCD
Mouse: Ntsr1 ^{GN220Gsat/Mmucl}	MMRRC	RRID: MMRRC_017266-UCD
Software and Algorithms		
LabVIEW	National Instruments	RRID: SCR_014325
Iris: 2 photon scanning software	N/A	https://sourceforge.net/projects/iris-scanning/
MATLAB	The MathWorks, Inc.	RRID: SCR_001622

(Continued on next page)

Continued

REAGENT or RESOURCE	SOURCE	IDENTIFIER
Calliope: Image processing software	N/A	https://svn.code.sf.net/p/iris-scanning/calliope/
NeuroMatic		RRID: SCR_004186
IGOR Pro	WaveMetrics	RRID: SCR_000325
Other		
Yellow LED (595 nm) for optogenetics	Prizmatix	UHP-T-595, http://www.prizmatix.com/uhp/uhp-mic-led-595.htm
Titanium Headplate	Leinweber et al. (2014)	Custom
Dichroic mirror	Chroma	Cat# ZT775sp-2p
Dichroic mirror	Semrock	Cat# F38-555SG
Virtual reality setup	Leinweber et al. (2014)	Custom

CONTACT FOR REAGENT AND RESOURCE SHARING

Further information and requests for resources and reagents should be directed to and will be fulfilled by the Lead Contact, Georg Keller (georg.keller@fmi.ch).

EXPERIMENTAL MODEL AND SUBJECT DETAILS**Animals and surgery**

Rabies tracing experiments ([Figure 1](#)) were performed on males and females of nine different mouse lines: C57BL/6J mice (n = 5), PV-Cre (*Pvalb*^{tm1(cre)Arbr}; n = 3) mice, VIP-Cre (*Vip*^{tm1(cre)Zjh}, n = 3), SST-Cre (*CR*^{tm1(cre)Zjh}, n = 4), CR-Cre (n = 3), Wfs1-Cre mice (*Wfs1*-Tg2-CreERT2; n = 3), Scnn1a-Cre (n = 4), 3 Rbp4-Cre (*Rbp4*^{KL100Gsat/Mmucl}; n = 3), Ntsr1-Cre (*Ntsr1*^{GN220Gsat/Mmucl}; n = 4). All mice used were between 71 and 370 days old. For all other experiments a total of 88 female C57BL/6J mice were used, 8-10 weeks old at the start of the experiment. All experiments were performed on healthy mice which were not used for prior procedures. Mice were group-housed in a vivarium (light/dark cycle: 12/12 hr). Female adult mice were mainly used to reduce aggression and dominance during group housing. All animal procedures were approved by and carried out in accordance with guidelines of the Veterinary Department of the Canton Basel-Stadt, Switzerland.

METHOD DETAILS**Surgery**

For all surgical procedures mice were anesthetized using a mix of fentanyl (0.05 mg/kg), medetomidine (0.5 mg/kg) and midazolam (5 mg/kg). Cranial windows were implanted as previously described ([Keller et al., 2012](#); [Leinweber et al., 2014](#)).

Rabies tracing

See [Figure 1](#) and [Figure S1](#). To initiate monosynaptic rabies tracing, either AAV2/1-Ef1a-TVA950-T2A-CVS11G or AAV2/1-Ef1a-DIO-TVA950-T2A-CVS11G (titer 2-4*10¹¹ GC/ml) was injected into V1 of C57BL/6J mice or of mice of different Cre lines, respectively, through a small craniotomy. Following the injection, the craniotomy was sealed with cyanoacrylate and the skin sutured. After 2-4 days the seal was removed and an EnvA-coated, glycoprotein-G deleted GCaMP6s rabies virus (referred to as EnvA-SAD Δ G-GCaMP6s, titer 1.5*10⁹ TU/ml, FACS titrated ([Wertz et al., 2015](#); [Wickersham et al., 2010](#))) was injected at the same location. For Wfs1-Cre mice, Cre expression was induced by intraperitoneal injection of 100 μ l tamoxifen (20mg/ml in saline) twice within a 24-48 hr interval 4 days after the AAV injection. Mice were sacrificed for histological staining 5-6 days after injection of the rabies virus. Mice were transcardially perfused for 10 min with phosphate buffered saline (PBS), followed by 10 min of perfusion with a solution of 4% paraformaldehyde (PFA) in PBS. Brains were then isolated and post-fixed for 24h in 4% PFA in PBS. The PFA solution was then exchanged for 30% sucrose in PBS, in which brains were immersed until they sank. Afterward, the brains were transferred to embedding medium (Tissue-Tek), frozen on dry ice and stored at -80°C before they were sectioned into 80 μ m coronal sections using a cryostat. Brain sections were placed in well-plates separately and kept free-floating in PBS. Each section was triple immunostained for rabies derived GFP (Abcam 13970), peptide linker 2A expressed by the AAV (Millipore #ABS31) and a neuron-specific nuclear protein NeuN (Millipore MAB377). The conjugated fluorescent labels of secondary antibodies were Alexa Fluor 488 (Jackson Immuno #703-545-155), Alexa Fluor 568 (ThermoFisher #A10042) and Alexa Fluor 647 (ThermoFisher #A31571), respectively. Stained sections were subsequently mounted on microscope slides and imaged using the ZEISS Axio Scan.Z1 slide scanner with 10x magnification. These images were then used to manually count the starter cells and rabies labeled cells throughout the brain. All the brain areas were defined as in ([Franklin and Paxinos, 2012](#)).

AAV tracing

See [Figures 2A-E](#) and [Figure S1C-E](#). A small craniotomy was made over A24b (centered on 0.3 mm lateral and 0.5 anterior of bregma) and AAV2/1-Ef1a-tdTomato-WPRE (titer 2.4×10^{11} GC/ml) and AAV2/1-Ef1a-eGFP-WPRE (titer 2.2×10^{11} GC/ml) were injected around bregma separated by 0.5 mm either along the anterior-posterior axis or the medio-lateral axis. The craniotomy was sealed with cyanoacrylate and the skin sutured. Three weeks later mice were sacrificed and perfused. Brain sections (80 μ m) were cut on a cryostat and mounted on microscope slides and imaged using the ZEISS Axio Scan.Z1 slide scanner with 10x magnification ([Figure 2B,C](#)), or with a confocal microscope ([Figure 2D](#)).

CRACM

See [Figures 2F](#) and [2G](#) and [Figure S1F-H](#). Adult (P90 – P150) C57BL/6J mice received AAV2/1-Ef1a-CatCh-eGFP (titer 2.3×10^{11} GC/ml) injections into the right A24b. After 3 - 5 weeks, mice were anesthetized with isoflurane and sacrificed. The brain was removed and coronal slices from right V1 prepared in ice-cold slicing solution (in mM: 87 NaCl, 2.5 KCl, 7 MgCl₂, 1.25 NaH₂PO₄, 25 NaHCO₃, 25 glucose, 75 sucrose, bubbled with 95% O₂/5% CO₂). 300 μ m thick slices were cut using a Campden Instruments 700 SMZ vibrating microtome. Slices were stored in ACSF (in mM: 125 NaCl, 2.5 KCl, 2 CaCl₂, 1 MgCl₂, 1.25 NaH₂PO₄, 26 NaHCO₃, and 25 glucose, pH 7.3, equilibrated with 5%CO₂/ 95%O₂) for 30 min at 35°C followed by up to 6 hr at room temperature until use. To quantify synaptic input from A24b to V1, whole-cell patch-clamp recordings were made from neurons in the visual cortex at room temperature (22 - 24°C). The intracellular solution contained (in mM): 120 potassium gluconate, 5 mM NaCl, 2 MgCl₂, 0.1 CaCl₂, 10 HEPES, 1.1 EGTA, 4 magnesium ATP, 0.4 disodium GTP, 15 sodium phosphocreatine and 0.1% Biocytin (pH 7.3 with KOH; 290 mOsm). The borders of the cortical layers were identified by cortical depth, neuron morphology, and the current responses of excitatory neurons. Layer 1 was identified by its low cell density. In early experiments identification of layer 4 and layer 5 was facilitated with the use of Rbp4-Cre mice injected with an AAV2/1-Ef1a-DIO-eGFP in V1.

A24b axons were activated selectively in layer 1 or layer 6 under a 60x 0.9 NA Olympus water immersion objective with 2 ms pulses from a blue LED at a power of 0.42 mW. Stimulation intensity was far below the threshold to trigger action potentials in postsynaptic neurons; the threshold for eliciting postsynaptic spikes was consistently above 4.0 mW. Postsynaptic responses were recorded at a holding potential of -70 mV. To determine the source of inputs, the area of stimulation centered on the region above or below the neuron in layer 1 and layer 6. No responses were observed when the stimulation was centered directly adjacent to layer 1 outside of cortex. In untransfected control mice LED stimulation did not evoke responses at stimulation intensities of 4.0 mW. All recordings were acquired and analyzed with IgorPro (WaveMetrics) using NeuroMatic.

Axonal imaging

See [Figures 3A-3C](#), [Figure 4](#), and [Figures S2A-G](#). A craniotomy was made over V1 and sealed with a 4 mm coverslip as previously described ([Leinweber et al., 2014](#)). Additionally, a small craniotomy was made over A24b (ipsilaterally, 0.3 mm lateral of bregma) and AAV2/1-Ef1a-GCaMP6f-WPRE (titer 1.0×10^{11} - 1.8×10^{12} GC/ml) was injected before the region was sealed with cyanoacrylate. A titanium head bar was fixed to the skull with dental cement. Prior to axon imaging, V1 was mapped with intrinsic signal imaging, as previously described ([Wertz et al., 2015](#)). Four weeks post injection, calcium signals in A24b axons were imaged using a modified Thorlabs B-Scope, as previously described ([Leinweber et al., 2014](#)). Illumination source was a pulsed infrared laser (Coherent Vision S) tuned to a wavelength of 990 nm. We used an 8 kHz resonance scanner (Cambridge Technology) for line scanning, which enabled frame rates of 40 Hz at 400 \times 750 pixel resolution. In addition, we used a piezo actuator (P-726 PIFOC, Physik Instrumente) to move the objective (Nikon 16x, 0.8 NA) in steps of 15 μ m between frames to acquire images at 4 different depths, thus reducing the effective frame rate to 10 Hz.

The behavioral virtual reality setup was as previously described ([Leinweber et al., 2014](#)). Briefly, head-fixed mice were free to run on an air-supported polystyrene ball. The rotation of the ball was restricted to the forward and backward directions using a pin, and was coupled to linear displacement in the virtual environment projected onto a toroidal screen surrounding the mouse. The screen covered a visual field of approximately 240 degrees horizontally and 100 degrees vertically. The virtual environment presented on the screen was a virtual tunnel with walls consisting of continuous vertical sinusoidal gratings. Mice were first exposed to a closed-loop condition, during which motion of the grating was coupled to the mouse's locomotion on the ball, and then exposed to an open-loop condition during which the visual flow of a previous closed-loop session was replayed to the mouse. The open-loop condition was followed by a dark session where all light sources including the virtual reality were turned off. To measure responses of A24b/M2 axons to the onset of darkness, all light sources were turned off for period of 2 s in a closed-loop session, in a subset of experiments. Additionally, visual feedback was perturbed during closed-loop conditions by stopping the gratings for a brief period (1 s) at random times, as described previously ([Keller et al., 2012](#)).

In vivo channelrhodopsin-2-assisted circuit mapping (ivCRACM)

See [Figure 3D-F](#) and [Figure S3](#). Viral injections and surgery were performed as described for the axon imaging with the exception that an AAV2/1-hSyn-ChrimsonR-tdTomato-WPRE (titer 3.0×10^{12} GC/ml) was injected into A24b and AAV2/1-Ef1a-GCaMP6f-WPRE (titer 1.0×10^{11} GC/ml) into V1. ChrimsonR stimulation and functional imaging of GCaMP6f expressing neurons was done by using a modified Thorlabs B-Scope. Illumination source for two-photon imaging was a pulsed infrared laser (Spectra physics) tuned to a wavelength of 990 nm. We used a 12 kHz resonance scanner (Cambridge Technology) for line scanning, which enabled frame rates of

60 Hz at 400×750 pixel resolution. In addition, we used a piezo actuator (Physik Instrumente) to move the objective (Nikon 16x, 0.8 NA) in steps of 15 μm between frames to acquire images at 4 different depths, thus reducing the effective frame rate to 15 Hz. Illumination source for ChrimsonR stimulation was a fast LED (UHP-T-595, Prizmatix) with a wavelength of 595 nm, which allowed for fast TTL triggered operation. Stimulation lasted for 1 s (20 Hz; 50% duty cycle) with an average power of 15 mW at random times during a closed-loop condition. For spectral filtering we used a dichroic mirror (ZT775sp-2p, Chroma) to combine the two-photon laser and stimulation light. A second long-pass dichroic mirror (F38-555SG, Semrock) was used to split the GFP emission from both illumination light sources. Light leak from the 595 nm stimulation LED was reduced by synchronizing the LED light output to the turnaround times of the resonant scanner (during which imaging data were not acquired). Lastly, amplified PMT signals were digitally bandpass filtered at 80 MHz to reduce the effect of ringing. Two-photon imaging of activity was otherwise performed as previously described (Leinweber et al., 2014).

Muscimol or ibotenic acid silencing of A24b

See Figure 3G-I and Figure S2H-L. Viral injections and surgery were performed as described above for axon imaging with the exception that AAV2/1-Ef1a-GCaMP6f-WPRE (titer 2.9×10^{12} GC/ml) was injected into V1. At the time of cranial window implant a small craniotomy over A24b was made and sealed with cyanoacrylate to allow for injections of muscimol or ibotenic acid preceding imaging without further need for surgery. Muscimol (at a concentration of 5 g/l) or ibotenic acid (13.5 g/l) was injected 15 min or 24 hr, respectively, prior to imaging at a volume of 50–100 nL at a depth of 500 μm .

Virtual reality and navigation task

See Figure 4, Figure 5 and Figure S4. Viral injections and surgery were performed as described above for axonal imaging. For training, mice were initially placed into a virtual environment with an infinite tunnel (identical to the one used for axonal imaging) for two training session on two consecutive days to allow the mice to get accustomed to the setup and virtual environment. Rotation of the spherical treadmill was restricted to forward and backward rotation using a pin. During subsequent training, rotation of the ball was no longer restricted and mice were free to rotate in the virtual environment in addition to moving forward and backward. The virtual reality consisted of a tunnel with a reward zone located at one end. The walls of the tunnel were textured with white circles on a black background in the first half of the tunnel and sinusoidal vertical stripes in the second half. Reaching the reward zone triggered a 5 s timeout during which the mouse could lick from a water spout for reward. After the timeout, the virtual environment was reset to the beginning of the tunnel to start the next trial. As the mouse's performance in the task improved, the length of the tunnel was gradually increased to keep the reward per hour at an approximately constant level of 100, throughout training. Mice were water restricted for the duration of the experimental series and were supplemented with water during early training sessions if they received less than 1 mL of total water reward. The weight of all mice was monitored daily to ensure that body weight would not drop below 80% of starting weight. A subset of mice were also exposed to an open-loop session on the first and last day of training. In the independent visual flow condition we replayed the visual flow generated by the same mouse in a preceding closed-loop session. In the no-visual flow condition, the reward location was still present in the virtual environment, but the walls of the environment were all uniformly gray.

For A24b axon stimulation experiments (Figure 5), viral injections and surgeries were performed as described above for axonal imaging with the exception that an AAV2/1-Ef1a-CatCh-eGFP (titer 2.3×10^{11} GC/ml) was injected into A24b of both hemispheres. Cranial windows were implanted over V1 of each hemisphere. Mice were trained and performed the same 2D navigation task as in Figure 4. A blue laser (473 nm) was directed either at monocular V1 or a blanking position using a pair of galvanometric mirrors. The stimulation (3 s, 25 Hz, 50% duty cycle) occurred once per traversal with a probability of 0.7 and at a random positions in the tunnel (located in a region between 20% and 70% of the length of the tunnel). A CCD camera was used to calibrate and select stimulation locations using custom-written software. Laser power was adjusted to 16 mW/mm² at the surface of the brain.

QUANTIFICATION AND STATISTICAL ANALYSIS

Data analysis

All imaging data were corrected for lateral brain motion using custom-written software. Regions of interest were automatically selected using a combination of independent component analysis and image segmentation as previously described (Mukamel et al., 2009). Fluorescence traces were calculated as the mean pixel value in each region of interest per frame and were median-normalized to calculate $\Delta F/F$. $\Delta F/F$ traces were filtered as previously described (Dombeck et al., 2007). The details of the statistical analysis are noted in the figure legends. We did not test the distribution of the data for normality.

Figure 2: The axon density profile was determined by calculating the mean fluorescence profile along the dorsal-ventral axis in V1 (lambda +0.4 mm). Individual traces were median normalized.

Figure 3: For stimulus-triggered fluorescence changes (onset responses, Figures 3, S2, and S3), fluorescence traces were mean-subtracted in a window preceding the stimulus onset (running onset: -1,900 ms to -1,500 ms; mismatch, visual flow or random: -500 ms to -100 ms). To correct for differences in running speed between the different conditions, individual trials were subsampled to match the distribution of running speeds across the conditions. Subsampling was performed by removing trials with the highest and lowest running speed iteratively until the distributions had matching means. Onset response latencies were determined by finding the onset of a persistent, significant deviation from baseline ($p < 0.01$, paired Student's t test, for at

least 1 s). Significance testing (Student's t test) was done in a window of 1 s centered on the peak of the distributions. To compare the distribution of running onset responses in A24/M2 axons and V1 neurons, we quantified the time to response as the time difference between the onset of the activity (more than 2 standard deviations above baseline for at least 1 s following this time) and the running onset. Each distribution of time differences was fitted with a two-term Gaussian model (Figure S2A). To quantify how visual flow influences running-related activity, we calculated a linear regression of the mean activity (in a window from 2 s to 4 s after running onset, averaged over all axons per imaging site) versus the average visual flow speed in a 1 s window that was varied between -10 s and 10 s. For each time step, we then calculated the average slope of the regression curves (averaged across imaging site) (Figure S2E). For the ivCRACM experiments, cells were considered to be driven by the stimulus light if the correlation between activity and stimulus was higher than 0.05. For the muscimol silencing experiments, the 50% of neurons most responsive to either running onset or mismatch were selected on two separate imaging time points preceding the baseline time point. Onset responses were then computed for these neurons for pre-muscimol (baseline, time point -1), muscimol inactivation of A24b (time point 0) and recovery (time point +1).

Figure 4: The activity $A(t)$ of each axon was correlated with different linear combinations of forward velocity $v(t)$ and rotation $r(t)$: $\alpha^*v(t) + \beta^*r(t)$, where $\alpha = \sin(\theta)$, $\beta = \cos(\theta)$. The interaction angle θ was varied from 0° to 180° in steps of 6° . For each axon an optimum interaction angle was determined, and axons were considered task-correlated if the correlation coefficient at optimum θ was higher than 0.005. Axons were classified as left (right) turning for an interaction angle between 6° and 66° (114° and 174°). Running forward ($\theta = 90^\circ$) and rotating without forward motion ($\theta = 0^\circ$, 180°) were excluded as they result in visual flow equal in magnitude in the left and right visual field. Learning was quantified as change in efficiency of moving toward the target. This was measured as the distance traveled toward the target normalized by the total distance traveled. Using this measure a random walk results in a performance of 0, movement in a straight line toward the target results in a score of 1.

Figure 5: To control for any unspecific effect of the stimulation on running speed, the stimulation effect of either left or right stimulation was normalized by subtracting the effect of bilateral stimulation.

DATA AND SOFTWARE AVAILABILITY

Requests for data and software should be directed to and will be fulfilled by the Lead Contact, Georg Keller (georg.keller@fmi.ch). Software for controlling the two-photon microscope and preprocessing of the calcium imaging data is available on <https://sourceforge.net/projects/iris-scanning>.